Atmos. Meas. Tech. Discuss., 6, 8311–8338, 2013
www.atmos-meas-tech-discuss.net/6/8311/2013/
doi:10.5194/amtd-6-8311-2013

Atmospheric Measurement Techniques Discussions

Lidar-based remote sensing of atmospheric boundary layer height over land and ocean

T. Luo[1,2], **R. Yuan**[2], **and Z. Wang**[1]

[1]University of Wyoming, Dept. Atmospheric Science, Laramie, WY, USA
[2]University of Science and Technology of China, School of earth and space science, Hefei, Anhui, China

Received: 17 July 2013 – Accepted: 21 August 2013 – Published: 9 September 2013

Correspondence to: T. Luo (tluo@uwyo.edu)

Published by Copernicus Publications on behalf of the European Geosciences Union.

Abstract

Atmospheric boundary layer (ABL) processes are important in climate, weather and air quality. A better understanding of the structure and the behavior of the ABL is required for understanding and modeling of the chemistry and dynamics of the atmosphere on all scales. Based on the systematic variations of ABL structures over different surfaces, different lidar-based methods were developed and evaluated to determine the boundary layer height and mixing layer height over land and ocean. With Atmospheric Radiation Measurement Program (ARM) Climate Research Facility (ACRF) micropulse lidar (MPL) and radiosonde measurements, diurnal and season cycles of atmospheric boundary layer depth and ABL vertical structure over ocean (TWP_C2 cite) and land (SGP_C1) are analyzed. The new methods are also applied to satellite lidar measurements. The derived global marine boundary layer structure database shows good agreement with marine ABL stratiform cloud top height.

1 Introduction

The atmospheric boundary layer (ABL) is the turbulent layer near the earth's surface (Stull, 1988). The heat, moisture or aerosols are trapped and vertically mixed within the ABL, and are exchanged with the free troposphere at the top of ABL. Therefore, boundary layer height (BLH) acts as a key length scale in weather, climate, and air quality models to determine turbulence mixing, vertical diffusion, convective transport and cloud formation (Garratt, 1992; Seibert et al., 2000; Stevens, 2002; Erickson et al., 2008; Kekkonen et al., 2012; Zilitinkevich, 2012; Ferrare et al., 2013). However, in operational forecast models, regional models, or global climate models, ABL is still poorly simulated due to complex processes at small temporal and spatial scales (Lenderink and Holtslag, 2000; Hannay et al., 2009; Wyant et al., 2010). Also modeled ABL is not fully evaluated due to the lack of reliable global BLH climatology database (Seidel et

AMTD
6, 8311–8338, 2013

al., 2010). Therefore, a better understanding of ABL structure and physical processes is required to improve model simulations.

Despite of its importance, BLH is difficult to be directly measured by standard meteorological measurements (Tombrou et al., 2007; Liu and Liang, 2010). Usually, BLH is indirectly diagnosed from analysis of thermodynamic variables, turbulence-related parameters or measuring concentrations of tracers, by using different definitions of BLH with respect to the various characteristics of ABL, as reviewed by Seidel et al. (2010). However, different definitions often give different BLH results and no standard BLH definition exists (Seidel et al., 2010). Also in-situ measurements are sparse especially over ocean. Over land, the limited sounding measurements may not be so representative for a large region due to surface inhomogeneity.

Satellite-based observations allow a non-traditional way to derive the global BLH climatology. A few studies have been done by using Global Positioning System radio occultation (GPS RO) measurements (Ratnam and Basha, 2010; Guo et al., 2011; Ao et al., 2012) or Cloud-Aerosol Lidar and Infrared Pathfinder Satellite Observation (CALIPSO) (McGrath-Spangler and Denning, 2013). GPS RO provides a valuable global view of height-resolved refractivity or moisture structure of ABL. However, GPS RO has very coarse resolutions (200m in vertical and ~200 km horizontal), and suffers several problems such as insufficient penetration into the lowest 500 m of atmosphere (Xie et al., 2012). CALIPSO has much finer vertical (30 m) and horizontal resolution (333 m) and is sensitive to boundary layer aerosols and clouds. Former studies showed that CALIPSO has the great ability to derive global BLH distributions (Jordan et al., 2010; McGrath-Spangler and Denning, 2012, 2013). However, the variance methods used in these studies often gave lower BLH than the other methods (will be shown in Sect. 2.3) and thus gave shallower BLH over ocean than other measurements (referring to Fig. 3 in McGrath-Spangler and Denning (2013) and Fig. 3 in Ratnam and Basha (2010)). And also the previous work mainly relay on in-situ measurements to evaluate the global BLH climatology (i.e., McGrath-Spangler and Denning, 2013). The

AMTD
6, 8311–8338, 2013

in-situ measurements are sparse and mainly limited over land, thus the limited evaluation results may be not so representative for global BLH distribution.

CALISPO could be a more powerful tool to provide the global BLH datasets. However, careful further evaluations are needed. Usually ABL has more content of aerosol than free upper atmosphere due to the limitation of capping inversion at the top of ABL and primary near-surface aerosol sources. Near surface aerosols are mixed within ABL by turbulence and convection, thus aerosol vertical distribution is heavily influenced by the thermal structure. Aerosol vertical structure is regarded as a good tracer to determine the BLH (Stull and Eloranta, 1984; Boers et al., 1984; Melfi et al., 1985; Boers and Eloranta, 1986). Lidar provides direct measurements of aerosol profiles within the ABL. Several methods, such as threshold method, gradient method, and variance method, have been developed to determine BLH by using lidar backscatter measurements (Emeis et al., 2008; Jordan et al., 2010). However, the detected aerosol layers are not always consistent with ABL thermodynamical structures because aerosol vertical structures are also affected by other factors. First, local aerosol vertical distributions are also influenced by horizontal transportation of aerosols besides of vertical turbulence mixing. Second, nighttime aerosol residual layer has weak linkages with ABL processes and is hard to distinguish the ABL aerosol (Ferrare et al., 2013), especially over land. Therefore, a careful evaluation of lidar based BLH is needed under different surface and thermal conditions in order to using it globally.

This study aims to improve lidar-based method to provide consistent BLH determinations as other methods based on thermo-dynamical properties. Long-term collocated lidar and radiosonde data is used to evaluate lidar-based BLH determination methods over land and ocean. The method is applied to space-borne lidar measurements to derive a global ABL structure database. Furthermore, BLH over ocean are further evaluated with lidar measured boundary layer stratiform cloud top heights, which is capped by the boundary layer top temperature inversion. Section 2 describes the ground- and satellite-based data and BLH identification methodology. Section 3 gives the results and some discussions, and Sect. 4 presents a brief conclusion.

AMTD
6, 8311–8338, 2013

2 Methodology

2.1 Data

2.1.1 Ground-based data

Atmospheric Radiation Measurement Program (ARM) Climate Research Facility (ACRF) radiosonde and micro pulse lidar (MPL) observations (Xie et al., 2010; Mather and Voyles, 2013) were used to investigate the boundary layer aerosol structure and to develop new lidar-based methods to determine the BLH over different surface. Nauru (TWP_C2, far ocean small island, 2007–2008) and Southern Great Plains (SGP_C1, land, 2007–2009) site were selected to represent typical land and ocean conditions.

1. Balloon-borne sounding system (SONDE) provides in situ measurements (vertical profiles) of temperature, water vapor and the wind speed and direction, at a frequency of 2 times per day at TWP_C2 and 4 times per day at SGP_C1.

2. Overlap corrected MPL cloud free signals were normalized to molecular backscattering to derive the total attenuated backscattering (TAB) for BLH determination. After overlap correction, the cloud is detected with the slope algorithm based on Wang and Sassen (2001), which uses the change in the slope of the backscattered signal as a function of height to identify the presence of cloud layers in the atmosphere, and uses several techniques to distinguish aerosol layers from cloud layers. Then, cloud-free signals (no cloud below 7 km) were averaged into 1-h resolution. Usually aerosol layer is lower than 5 km, thus signals within 5 and 6 km are selected to calibrate the observed TAB profile with molecular backscattering coefficients, which are estimated with SONDE temperature and pressure profiles. Due to uncertainties in overlap correction below 500 m, MPL TABs below 500 m are not used in this study.

AMTD
6, 8311–8338, 2013

2.1.2 Satellite-base data

To build global marine BLH database, multiple remotely sensed and operational meteorological datasets over far ocean during the period of June 2006 to December 2010 are used, including:

1. CALIPSO level 1b data: CALIPSO is a polarization-sensitive lidar capable of measuring backscatter intensity at wavelengths of 532 and 1064 nm. CALIOP level 1B data (horizontal resolution of 333 m along the track) are calibrated and geolocated 532 and 1064 nm total attenuated backscatter and 532nm perpendicular polarization component (Hostetler et al., 2006).

2. CloudSat 2B GEOPROF: Cloudsat carries a 94 GHZ cloud profiling radar (CPR) with horizontal resolution of 1.3 km cross track and 1.7 km along track. The 2B-GEOPROF product contains the cloud mask information that identifies where hydrometeors occur in individual profiles over the instrument noise floor (Mace, 2007).

3. ECMWF-AUX: contains temperature and pressure profiles from the European Centre for Medium-Range Weather Forecasts (ECMWF) operational analysis interpolated in time and space to the CloudSat track (Partain, 2004).

The cloud is identified by combining CloudSat GEOPROF product and CALIPSO level 1B data (detailed in Wang, et al, 2008, and Loknath et al, 2010). After cloud identifying, clear-sky lidar profiles within a 25km box were averaged to increase signal-to-noise ratio (SNR). In this study, only clear-sky data within 50N and 50S and 200km away from continents were used.

2.2 BLH determination methodology with SONDE measurements

The literatures contain many methods for estimating BLH (see reviews in Seidel et al., 2010 for details). The main design of these methods is based on some common

AMTD
6, 8311–8338, 2013

characteristics of ABL. Usually a capping inversion exists at the top of the ABL, which prevents the vertical transportations of heat, humidity and pollutions. Below the capping inversion, usually the ABL is assumed to be well mixed. These different methods tried to identify ABL top characteristics to determine BLH with different variables such as temperature or humidity gradient, but often give different BLHs (Seidel et al., 2010).

For SONDE, Seidel et al. (2010) recommended either the parcel method or the Richardson number (*RI*) method to be the most reliable method under convective conditions, whereas the *RI* method was regarded as the most suitable method under conditions with mechanically produced turbulence. The parcel method determines the height of intersection of the actual potential temperature profile with the dry-adiabatic ascent starting at near-surface temperature (Holzworth, 1964, 1967, 1972). The *RI* method determines the BLH as the height at which *RI* is larger than the critical value (= 0.25), here, *RI* defined as (Vogelezang and Holtslag, 1996)

$$RI = \frac{g\,z(\theta(z) - \theta(s))}{\theta(s)[(u(z) - u(s))^2 + (v(z) - v(s))^2]}. \quad (1)$$

Good agreements were found for BLH derived by the parcel method and the *RI* method, whereas sometimes parcel model is inapplicable, i.e., in the afternoon, due to the decrease in near surface temperature (Hennemuth and Lammert, 2006). The *RI* method is suitable for both stable and convective boundary layers. This method relates the derived BLH to ABL processes – surface heating, wind shear and capping inversion, thus gives the BLH more physical meaning. Also *RI* method is not strongly dependent on sounding vertical resolution, giving no-negative BLH. Therefore the *RI* method will be adopted in this study as the best estimation for lidar based BLH evaluations.

2.3 BLH detection methodology with ground-based lidar measurements

For lidar observations, using different characteristics of returned backscatter to determine the BLH may give different characteristic scale of ABL (Emeis et al., 2008). Five methods were demonstrated in Fig. 1a–e respectively. The threshold method (Fig. 1a)

AMTD
6, 8311–8338, 2013

sets the BLH at the height where lidar aerosol signal above certain threshold and will be detailed further in the next section. The gradient method (Fig. 1b), log-gradient method (Fig. 1c) and second derivation method (Fig. 1c) determine the BLH at the height corresponding to the minimum of the gradient, log-gradient and second derivation of lidar backscattering respectively (Emeis et al., 2008). The variance method determines the BLH as the maximum of the variance profile (Jordan et al., 2010). As shown in Fig. 1a, the threshold method gives the highest BLH; the gradient and log-gradient method gives the second highest BLH; and the second derivation and variance method gives the lowest BLH. Therefore a careful evaluation of their performance is needed. In this study, we'd like to identify the BLH as the height up to which the influence of the surface forcing on aerosol content is detectable, and we also try to find suitable lidar-based methodology under different conditions to minimize the difference between lidar-derived BLH and traditionally SONDE defined BLH.

Aerosol vertical distribution is strongly influenced by the ABL thermal structures, which are different over land and ocean, as shown in Fig. 2. Over land, sharp gradient in water vapor mixing ratio and potential temperature could be found near the ABL top. Below the capping inversion layer, the land ABL is well mixed and the potential temperature and mixing ratio is nearly constant. Therefore the mixing layer height (MLH) could be treated as the BLH. The aerosol loading in mixing layer is higher than upper layer, which leads to a sharp gradient in TAB near the mixing layer top. On the contrast, the deep marine boundary layer (MBL) is more likely to be decoupled (Wood and Bretherton, 2004). As shown in Fig. 2, in deep MBL cases (BLH between 1.5 and 2 km), mixing layer only occupies about 30 % of the total ABL. MLH is much shallower than BLH and cannot be treated as BLH under this situation. Sharp gradient near the mixing layer top could be found in humidity, temperature and TAB. In shallow MBL cases (BLH between 0.8 and 1.2 km), the ABL structure is quite similar to that over land, but not so well mixed. The gradients in humidity, temperature or TAB at the ABL top are not as sharp as those over land.

AMTD
6, 8311–8338, 2013

The diurnal boundary layer aerosol structures over different surfaces were further investigated. Figure 3 shows the averaged diurnal cycles of boundary layer aerosol structures over land and ocean in different seasons. The corresponding SONDE-derived diurnal cycle of BLHs were also overlaid as a reference.

Over the oceans, the diurnal cycles of BLH over ocean are very weak in all seasons, because the daily cycle of the surface sensible heat flux is weak and often a persistent boundary layer with a capping inversion can be observed. The aerosol content has more concentrations below BLH, because the major source of marine aerosol is sea salt production by sea-spray processes at sea surface. The sea salt aerosols will be vertical transported through turbulent mixing processes and be capped by inversion at the boundary layer top. Also the MBL shows decoupled structure when deeper. The lower layer near surface is well mixed and has much higher aerosol loading than the upper decoupled layer.

Over land, boundary layer has much stronger diurnal cycle especially in MAM and JJA at the SGP site, corresponding to the sensible heat flux variations at the surface. The aerosol layer structure over land is more complicated than that over ocean, because aerosol here is not all locally produced. The aerosol layer over land is usually higher than BLH, mainly due to background aerosols or elevated aerosol layer. Especially during night, when turbulence is weak, the residual layer still contains very high aerosol loadings and it is hard to find systematic characteristics to distinguish the boundary layer aerosol and the lofted aerosol. However, usually a sharp gradient of aerosol backscattering can be expected near the convective boundary layer top during daytime.

Therefore, considering their systematic different characteristics, different methodologies are needed for identifying BLH over ocean and land, as shown in Figs. 4 and 5.

Over ocean, the threshold method could be used to determine the BLH. BLH is defined at where TAB $> \beta'_{\mathrm{thr}}$, here β'_{thr} is defined as

$$\beta'_{\mathrm{thr}} = \beta'_{\mathrm{m}} + 2\,\mathrm{MBV}, \quad (2)$$

AMTD
6, 8311–8338, 2013

where, β'_m is the attenuated molecular backscattering, estimated based on temperature and pressure profiles from SONDE data or from other sources; MBV is the measured backscatter variation, estimated as the standard deviation of measured attenuated backscatter coefficients within 5 to 7 km.

BLH is searched from top down as the first three points larger than β'_{thr}. To remove the possible elevated layer, we keep searching the strong peak near the BLH. If there exists a strong peak near formerly identified BLH, the profile will be identified as the elevated layer case and the layer base (where gradient changes its sign) is identified and treated as BLH.

Over land, the gradient method could be used to determine the BLH (or MLH) at daytime, by determining the first minimum peak of the TAB gradient smaller than threshold ($= 4 \cdot d\beta'_m$, $d\beta'_m$ is the gradient of molecular backscattering) from bottom upward. Also the gradient method could be used to determine the marine MLH, as the dashed blue line in Fig. 4.

2.4 Methodology for space-borne lidar

BLH can be determined with collocated CALIPSO level 1B data by an improved threshold method due to its lower signal-to-noise ratio. For molecular attenuation corrected signals, the threshold β'_{thr} is still chosen as

$$\beta'_{thr} = \beta'_m + 2 \cdot \mathrm{MBV}. \quad (3)$$

Here,β'_m is the molecular backscattering, estimated by temperature and pressure profiles from ECMWF-AUX products; MBV is the measured backscatter variation, estimated as the standard deviation of measured attenuated backscatter coefficients from 30 to 40 km.

Considering the poor SNR in 532 nm channels, 532 nm (β'_{532}) and 1064 nm (β'_{1064}) attenuated backscatter were combined to determine the aerosol layer, because β'_{1064} is less noised and molecular attenuated. For each aerosol layer detected by the threshold method, it should exist in the both channels.

AMTD
6, 8311–8338, 2013

The detailed aerosol layer identification scheme is as follows:

1. For each height, compute molecular backscattering coefficients β'_{m}, two-way transmittances T^2_{m} and MBV at 532 and 1064 nm; and then the corrections for molecular attenuations were applied to signals, as

$$\beta' = \beta'_{obs} / T^2_{m}. \quad (4)$$

Here, β'_{obs} is the measured signal; β' is the corrected signal.

2. Build up aerosol masks at each channel. To compensate the attenuation incurred within and bellow the aerosol layers, the estimated aerosol backscattering coefficients β_e were used to identify layers. The $\beta_e$were computed with the forward method (Klett, 1981; Fernald, 1983; Young and Vaughan, 2009) by assuming layer top at 8 km. Lidar ratios (S) were chosen as 25 (532 nm) and 40 (1064 nm). While retrieving at certain level, β_e will be set to zero if $\beta_e + \beta_m$ is smaller than $(\beta'_m + 2\,\mathrm{MBV})/T^2_e$ (here, T^2_e is the estimated transmittances of aerosols with β_e). Then, aerosol mask will set to be 1 for each height bin where $\beta_e > 0$.

3. Refine the aerosol mask by combining 532 and 1064 nm aerosol mask profiles. First, for each wavelength, we remove the aerosol layer with less than 3 points. Then we combine 532 and 1064 nm aerosol mask profiles and set the new aerosol mask to be 1 if mask in any of profiles equals to 1 at certain height. Finally, to get more accurate aerosol layer top, a 3-points moving smooth is applied to β'_{532} profiles. And then the aerosol layer top is defined as the highest points extending from the certain aerosol layer where β'_{532} is larger than β'_{thr} in Eq. (1) and color ratio (1064 nm/532 nm) is larger than 0.06. Then, a final check with elevated layer will be done. Only the lowest layer is identified as boundary aerosol layer. This screen removes the elevated layer which has a gap between the boundary aerosol layer. However there are still a few cases that elevated layer connected with the boundary aerosol layer. Therefore, if the initial identified BLH is higher than 2.5 km

AMTD
6, 8311–8338, 2013

and there exists strong peak closed to BLH, the elevated layer is exist. Then, the elevated layer base (where gradient change its sign) will be used as the BLH.

4. Identify MLH by the gradient method. The gradient of β_e is calculated after three points moving smoothing. Then MLH is determined from bottom up as the first point with β_e gradient larger than 4 times of the molecular backscattering gradient.

3 Results and discussion

3.1 Validation

The lidar-based algorithms discussed above are applied to MPL observations at TWP_C2 (daytime and nighttime, 11 782 profiles) and SGP_C1 cite (daytime only, 5926 profiles). 3-h averaged BLH were collocated with SONDE observations for comparison, as shown in Fig. 6a and b. MPL derived BLHs show good agreements SONDE determined BLHs. Over ocean, the bias and mean square error (MSE) of MPL derived BLH is -0.12 ± 0.24 km, and 83 % of points have a percentage difference less than 30 %. Over land, the bias and MSE is -0.04 ± 0.27 km. 74 % of points have a percentage difference less than 30 %. However, there are a few points with large discrepancy between the two methods. Over ocean (Fig. 6a), there are a few points with MPL derived BLH much lower than SONDE derived BLH, which is mainly due to the overlap issues. Over land (Fig. 6b), unidentified elevated aerosol layers result in a few points with MPL derived BLH much higher than SONDE derived BLH. Under strong convection situation over land, the gradient method often underestimates BLH according to SONDE results. But the threshold method performs better under this situation. Therefore, no single approach can cover all situations over land.

The diurnal and seasonal cycles of BLH from 1-h averaged MPL observations also show good agreement with those from SONDE, especially over ocean (Fig. 7). Over land, the MPL derived BLH accords well in warm seasons but shows a positive bias (+0.296 km) in cold seasons. This suggests that lidar-based BLH identification over

AMTD
6, 8311–8338, 2013

land could be further improved. During night, aerosol structure is less correlated with boundary layer thermo-dynamical structure, especially under cold surface temperature. And another issue is the overlap correction because the nighttime BLH is often near to or is lower than 500 m.

The lidar-based algorithms were also applied to CALIPSO observations over global ocean to derived 4-yr global ocean BLH datasets. Marine stratiform clouds were a good proxy to estimate marine BLH from satellite-retrieve cloud-top heights in previous studies (Minnis et al., 1992; Wood and Bretherton, 2004; Ahlgrimm and Randall, 2006; Zuidema et al., 2009; Karlsson et al., 2010). Therefore, marine stratiform cloud top height was used to evaluate the large database in this study. Cloud top height and cloud type was provided by Cloudsat 2B-CLD-CLASS-LIDAR data (Wang, 2011). Stratifrom cloud height was collocated and averaged into the same 25 km grid box as described in Sect. 2.4. Only the cases with cloud fraction between 0.1 and 0.7 were considered. As shown in Fig. 6c, CALIPSO derived BLH shows good agreement with marine stratiform cloud height. The bias and MSE of CALIPSO derived BLH is -0.08 ± 0.37 km. 75 % of points have a percentage difference less than 30 %.

3.2 Discussion

Over ocean, former studies showed the cloud-topped MLH is shallower than BLH when deepening, and the ABL is not well mixed above MLH (Wood and Bretherton, 2004). Bretherton and Wyant (1997) showed the decoupling structure under cloudy condition is mainly driven by an increasing ratio of the surface latent heat flux to the net radiative cooling in the cloud. And other factors, such as drizzle, the vertical distribution of radiative cooling in the cloud, and sensible heat fluxes, only play less important roles. However, early observations are mainly limited to specific case studies (Wood and Bretherton, 2004). The decoupling mechanisms of MBL are still not well understood, especially for none cloud-toped MBL. Lidar can provide MLH and BLH simultaneously to further study the decoupling.

AMTD
6, 8311–8338, 2013

Figure 8a–c shows the MBL structure in terms of water vapor, temperature, and aerosol TAB as a function of BLH determined from ground-based SONDE measurements during 2007–2008 at the TWP_C2 site. Figure 8a and b show that the MPL-derived MLH is coincident with sharp gradients of temperature and humidity. Mixing layer is moister and unstable than the ABL above the MLH (decoupled from near surface mixing layer). The decoupling becomes clear when BLH is deeper than 1 km. Figure 8c shows the aerosol structure changing with SONDE determined BLH systematically. The aerosol intensity gradients at MLHs are consistent with temperature and water vapor jumps. Therefore the gradient method is reliable to identify the marine MLH. To further illustrate this point, CALIPSO observations within a 10° latitude × 20° longitude box centered at TWP_C2 cite are shown in Fig. 8d and e. It is clear that marine ABL aerosols show distinct signatures for BLH and MLH. Figure 9d shows more aerosol contents in mixing layer than the rest of ABL in terms of lidar signal intensities. Combined with two wavelength CALIPSO measurements, Fig. 8e provides the color ratio (1064 nm/532 nm) of aerosols. The larger the color ratio is, the larger the aerosol particle size is. Thus, Fig. 8e shows that the mixing layer has relatively larger particle size than the rest of the ABL, which is consistent with higher water vapor mixing ratio in the mixing layer. These results showed that the decoupling occur frequently under cloud-free conditions. Similar structure could also be found over global ocean. With the global MBL BLH and MLH datasets from CALIPSO measurements, factors controlling MBL decouple structure over global ocean will be further studied in the future.

4 Conclusions

In this study, lidar-based methods are developed to provide consistent BLH and MLH determinations as those with temperature profiles. The results are evaluated with multi-year data. A global lidar-based MBL structure database was created.

With ACRF MPL and radiosonde measurements, diurnal cycles of boundary layer aerosol structures over land and ocean are investigated and compared. The results

AMTD
6, 8311–8338, 2013

showed systematically different characteristics requiring different approaches for land and ocean to determine the BLH and MLH with lidar aerosol measurements. Over ocean, MBL shows decoupled structure. The aerosol layer top shows good according with BLH and could be easily identified by the threshold method. And the MLH could be identified by gradient methods. Over land, the boundary layer aerosol structure is very complicated due to several reasons, such as that the turbulence in nocturnal boundary layer is very weak and the residual layer still has very high aerosol loading, or that the aerosol over land is not dominantly locally produced, thus there are elevated aerosol layers transported from non-local sources, etc. The aerosol layer top is usually higher than BLH. The daytime BLH could be identified by gradient method using lidar observations.

Comparison between MPL derived BLH and Sonde derived BLH shows good agreements. Over ocean, the bias and MSE of MPL derived BLH is -0.12 ± 0.24 km and 83 % of points have relative error smaller than 30 %. Over land, the bias of MPL derived BLH is -0.04 ± 0.27 km and 74 % of points have relative error smaller than 30 %. However, the BLH identification over land still needs further improvements, especially during nighttime. During night, aerosol structure is less correlated with boundary layer thermo-dynamical structure. This is a general weakness of using lidar aerosol measurements for BLH determination. It will be our future work to further improve the BLH identification over land.

The improved lidar-based method was further applied to CALIPSO cloud-free observations and a global marine BLH and MLH database were developed. The BLHs was further evaluated with global marine stratiform cloud top. The mean bias and MSE of CALIPSO derived BLH is -0.08 ± 0.37 km and 75 % of points have relative error smaller than 30 %. This indicates that CALIPSO aerosol measurements offer reliable BLH over oceans with our method. The gradient method applied to CALIPSO aerosol measurements also provide reliable MLHs, which corresponds well with MBL potential temperature and water vapor structure. The global marine ABL structure database developed in this study is useful for model evaluations and for process study to improve

AMTD
6, 8311–8338, 2013

the ABL simulations in the weather, climate, and air quality models. The results show that MBL are often decoupled under cloud free conditions. With the dataset, we will further understand the MBL decoupling structure and related mechanisms.

Acknowledgements. This research was funded by NASA grant NNX10AN18G, and also partially supported by DOE DE-SC0006974 as part of the ASR program. Tao Luo's effort was also supported by National Natural Science Foundation of China (41105018). The authors acknowledge the US Department of Energy ARM Climate Research Facility.

References

Ahlgrimm, M. and Randall, D. A.: Diagnosing Monthly Mean Boundary Layer Properties from Reanalysis Data using a Bulk Boundary Layer Model, J. Atmos. Sci., 63, 998–1012, 2006.

Ao, C. O., Waliser D. E., Chan, S. K., Li, J.-L., Tian, B., Xie, F., and Mannucci, A. J.: Planetary boundary layer heights from GPS radio occultation refractivity and humidity profiles, J. Geophys. Res., 117, D16117, doi:10.1029/2012JD017598, 2012.

Boers, R. and Eloranta, E. W.: Lidar Measurements of the Atmospheric Entrainment Zone and Potential Temperature Jump across the Top of the Mixed Layer, Bound.-Lay. Meteorol., 34, 357–375, 1986.

Boers, R., Eloranta, E. W., and Coulter, R. L.: Lidar Observations of Mixed Layer Dynamics: Tests of Parametrized EntrainmentModels of Mixed Layer Growth Rate, J. Clim. Appl. Meteorol., 23, 247–266, 1984.

Bretherton, C. S. and Wyant, M. C.: Moisture transport, Lower-tropospheric Stability, and Decoupling of Cloud-topped Boundary Layers, J. Atmos. Sci., 54, 148–167, 1997.

Emeis, S., Schafer, K., and Munkel, C.: Surface-based Remote Sensing of the Mixing-layer Height – a Review, Meteorol. Z., 17, 621–630, 2008.

Erickson III, D. J., Oglesby, R. J., Elliott, S., Steffen, W., and Brasseur, G.: Challenges in Earth System Modeling: Approaches and Applications, Paper 64, US Department of Energy Publications, http://digitalcommons.unl.edu/usdoepub/64 (last access: 29 August 2013), 2008.

Fernald, R. G.: Analysis of atmospheric lidar observations some comments, Appl. Optics, 23, 652–653, 1983.

AMTD

6, 8311–8338, 2013

Ferrare, R., Clayton, M., Turner, D., Newsom, R., and Scarino, A.: Raman Lidar Retrievals of Mixed-layer Heights over the TWP Darwin and SGP Sites, 4th Atmospheric System Research (ASR) Science Team Meeting, Potomac, Maryland, 2013.
Garratt, J. R.: The Atmospheric Boundary Layer, Cambridge Univ. Press, Cambridge, UK, 335 pp., 1992.
Guo, P., Kuo, Y.-H., Sokolovskiy, S. V., and Lenschow, D. H.: Estimating Atmospheric Boundary Layer Depth using COSMIC Radio Occultation Data, J. Atmos. Sci., 68, 1703–1713, 2011.
Hannay, C., Williamson, D. L., Hack, J. J., Kiehl, J. T., Olson, J. G., Klein, S. A., Bretherton, C. S., and Köhler, M.: Evaluation of Forecasted Southeast Pacific Stratocumulus in the NCAR, GFDL, and ECMWF models, J. Climate, 22, 2871–2889, 2009.
Hennemuth, B. and Lammert, A.: Determination of the Atmospheric Boundary Layer Height from Radiosonde and Lidar Backscatter, Bound.-Lay. Meteorol., 120, 181-200, 2006.
Hostetler, C., Liu, Z., Reagan, J., Vaughan, M., Osborn, M., Hunt, W. H., Powell, K. A., and Trepte, C.: CALIOP Algorithm Theoretical Basis Document – Part 1: Calibration and Level 1 Data Products, PC-SCI-201, Release 1.0, NASA Langley Research Center, Hampton, VA, 2006.
Holzworth, G. C.: Estimates of Mean Maximum Mixing Depths in the Contiguous United States, Mon. Weather Rev., 92, 235–242, 1964.
Holzworth, G. C.: Mixing depths, Wind speeds and Air pollution Potential for Selected Locations in the United States, J. Appl. Meteorol., 6, 1039–1044, 1967.
Holzworth, G. C.: Mixing depths, Wind speeds, and Potential for Urban Pollution throughout the Contiguous United States, Office of Air Programs Publ. AP-101, EPA, Research Triangle Park, NC, 118 pp., 1972.
Jordan, N. S., Hoff, R. M., and Bacmeister, J. T.: Validation of Goddard Earth Observing System-version 5 MERRA Planetary Boundary Layer Heights using CALIPSO, J. Geophys. Res., 115, D24218, doi:10.1029/2009JD013777, 2010.
Karlsson, J., Svensson, G., Cardoso, S., Teixeira, J., and Paradise, S.: Subtropical Cloud-Regime Transitions: Boundary Layer Depth and Cloud-Top Height Evolution in Models and Observations, J. Appl. Meteorol. Clim., 49, 1845–1858, 2010.
Klett, J.: Stable analytical inversion solution for processing lidar returns, Appl. Optics, 20, 211–220, doi:10.1364/AO.20.00, 1981.
Kukkonen, J., Olsson, T., Schultz, D. M., Baklanov, A., Klein, T., Miranda, A. I., Monteiro, A., Hirtl, M., Tarvainen, V., Boy, M., Peuch, V.-H., Poupkou, A., Kioutsioukis, I., Finardi, S., Sofiev,

AMTD
6, 8311–8338, 2013

M., Sokhi, R., Lehtinen, K. E. J., Karatzas, K., San José, R., Astitha, M., Kallos, G., Schaap, M., Reimer, E., Jakobs, H., and Eben, K.: A review of operational, regional-scale, chemical weather forecasting models in Europe, Atmos. Chem. Phys., 12, 1–87, doi:10.5194/acp-12-1-2012, 2012.

Lenderink, G. and Holtslag, A. A. M.: Evaluation of Kinetic Energy Approach for Modeling Turbulent Fluxes in Stratocumulus, Mon. Weather Rev., 128, 244–258, 2000.

Liu, S. and Liang, X.-Z.: Observed Diurnal Cycle Climatology of Planetary Boundary Layer Height, J. Climate, 22, 5790–5809, 2010.

Loknath, A., Wang, Z., and Liu, D.: Microphysical Properties of Antarctic Polar Stratospheric Clouds and their Dependence on Tropospheric Cloud Systems, J. Geophys. Res., 15, D00H18, doi:10.1029/2009JD012125, 2010.

Mace G.: Level 2 GEOPROF Product Process Description and Interface Control Document Algorithm version 5.3, http://www.cloudsat.cira.colostate.edu/ICD/2B-GEOPROF/2BGEOPROF_PDICD_3.0.pdf (last access: 29 August 2013), 2007.

Mather, J. H. and Voyles, J. W.: The Arm Climate Research Facility: A Review of Structure and Capabilities, B. Am. Meteorol. Soc., 94, 377–392, 2013.

McGrath-Spangler, E. L. and Denning, A. S.: Estimates of North American Summertime Planetary Boundary Layer Depths Derived from Space-borne Lidar, J. Geophys. Res., 117, D15101, doi:10.1029/2012JD017615, 2012.

McGrath-Spangler, E. L. and Denning, A. S.: Global Seasonal Variations of Midday Planetary Boundary Layer Depth from CALIPSO Space-borne LIDAR, J. Geophys. Res.-Atmos., 118, 1226–1233, 2013.

Melfi, S. H., Sphinhirne, J. D., Chou, S. H., and Palm, S. P.: Lidar Observations of the Vertically Organized Convection in the Planetary Boundary Layer over the Ocean, J. Clim. Appl. Meteorol., 24, 806–821, 1985.

Minnis, P., Heck, P. W., Young, D. F., Fairall, C. W., and Snider, J. B.: Stratocumulus Cloud Properties Derived from Simultaneous Satellite and Island-based Instrumentation during FIRE, J. Appl. Meteorol., 31, 317–339, 1992.

Partain, P.: Cloudsat ECMWF-AUX Auxiliary Data Process Description and Interface Control Document, http://www.cloudsat.cira.colostate.edu/ICD/ECMWFAUX/ECMWF-AUX_PDICD_3.0.pdf (last access: 29 August 2013), 2004.

AMTD
6, 8311–8338, 2013

Ratnam, M. V. and Basha, S. G.: A Robust Method to Determine Global Distribution of Atmospheric Boundary Layer Top from COSMIC GPS RO Measurements, Atmos. Sci. Lett., 11, 216–222, 2010.
Seibert, P., Beyrich, F., Gryning, S.-E., Joffre, S., Rasmussen, A., and Tercier, P.: Review and Intercomparison of Operational Methods for the Determination of the Mixing Height, Atmos. Environ., 34, 1001–1027, 2000.
Seidel, D. J., Ao, C. O., and Li, K.: Estimating Climatological Planetary Boundary Layer Heights from Radiosonde Observations: Comparison of Methods and Uncertainty Analysis, J. Geophys. Res., 115, D16113, doi:10.1029/2009JD013680, 2010.
Stevens, B.: Entrainment in Stratocumulus Topped Mixed Layers, Q. J. Roy. Meteorol. Soc., 128, 2663–2689, 2002.
Stull, R. B.: An Introduction to Boundary Layer Meteorology, Kluwer Academic Publishers, Norwell, MA, 1988.
Stull, R. B. and Eloranta, E. W.: Boundary Layer Experiment 1983, B. Am. Meteorol. Soc., 65, 450–456, 1984.
Tombrou, M., Dandou, A., Helmis, C., Akylas, E., Angelopoulos, G., Flocas, H., Assimakopoulos, V., and Soulakellis, N.: Model Evaluation of the Atmospheric Boudary Layer and Mixed-layer Evolution, Bound.-Lay. Meteorol., 124, 61–79, 2007.
Vogelzang, D. H. P. and Holtslag, A. A. M.: Evaluation and Model Impacts of Alternative Boundary-Layer Height Formulations, Bound.-Lay. Meteorol., 81, 245–269, 1996.
Wang, Z.: 2B-CLDCLASS-LIDAR Interface Control Document, http://www.cloudsat.cira.colostate.edu/icd_pdf.php?avid=36&pvids=12 (last access: 29 August 2013), 2011.
Wang, Z. and Sassen, K.: Cloud Type and Macrophysical Property Retrieval Using Multiple Remote Sensors, J. Appl. Meteorol., 40, 1665–1682, 2001.
Wang, Z., Stephens, G., and Deshler, T.: Association of Antarctic polar stratospheric cloud formation on tropospheric cloud systems, Geophys. Res. Lett., 35, L13806, doi:10.1029/2008GL034209, 2008.
Wood, R. and Bretherton, C. S.: Boundary Layer Depth, Entrainment, and Decoupling in the Cloud-Capped Subtropical and Tropical Marine Boundary Layer, J. Climate, 17, 3576–3588, 2004.
Wyant, M. C., Wood, R., Bretherton, C. S., Mechoso, C. R., Bacmeister, J., Balmaseda, M. A., Barrett, B., Codron, F., Earnshaw, P., Fast, J., Hannay, C., Kaiser, J. W., Kitagawa, H., Klein, S. A., Köhler, M., Manganello, J., Pan, H.-L., Sun, F., Wang, S., and Wang, Y.: The PreVOCA

AMTD
6, 8311–8338, 2013

experiment: modeling the lower troposphere in the Southeast Pacific, Atmos. Chem. Phys., 10, 4757–4774, doi:10.5194/acp-10-4757-2010, 2010.

Xie, F., Wu, D. L., Ao, C. O., Mannucci, A. J., and Kursinski, E. R.: Advances and limitations of atmospheric boundary layer observations with GPS occultation over southeast Pacific Ocean, Atmos. Chem. Phys., 12, 903–918, doi:10.5194/acp-12-903-2012, 2012.

Xie, S., McCoy, R. B., Klein, S. A., Cederwall, R. T., Wiscombe, W. J., Jensen, M. P., Johnson, K. L., Clothiaux, E. E., Gaustad, K. L., Long, C. N., Mather, J. H., McFarlane, S. A., Shi, Y., Golaz, J.-C. , Lin, Y., Hall, S. D., McCord, R. A., Palanisamy, and Turner, D. D.: Clouds and More: ARM Climate Modeling Best Estimate Data, B. Am. Meteorol. Soc., 91, 13–20, 2010.

Young, S. A. and Vaughan, M. A.: The Retrieval of Profiles of Particulate Extinction from Cloud-Aerosol Lidar Infrared Pathfinder Satellite Observations (CALIPSO) Data: Algorithm Description, J. Atmos. Ocean. Tech., 26, 1105–1119, 2009.

Zilitinkevich, S. S.: The Height of the Atmospheric Planetary Boundary layer: State of the Art and New Development, National Security and Human Health Implications of Climate Change, Springer, the Netherlands, 147–161, 2012.

Zuidema, P., Painemal, D., de Szoeke, S., and Fairall, C.: Stratocumulus Cloud-Top Height Estimates and Their Climatic Implications, J. Climate, 22, 4652–4666, 2009.

AMTD
6, 8311–8338, 2013

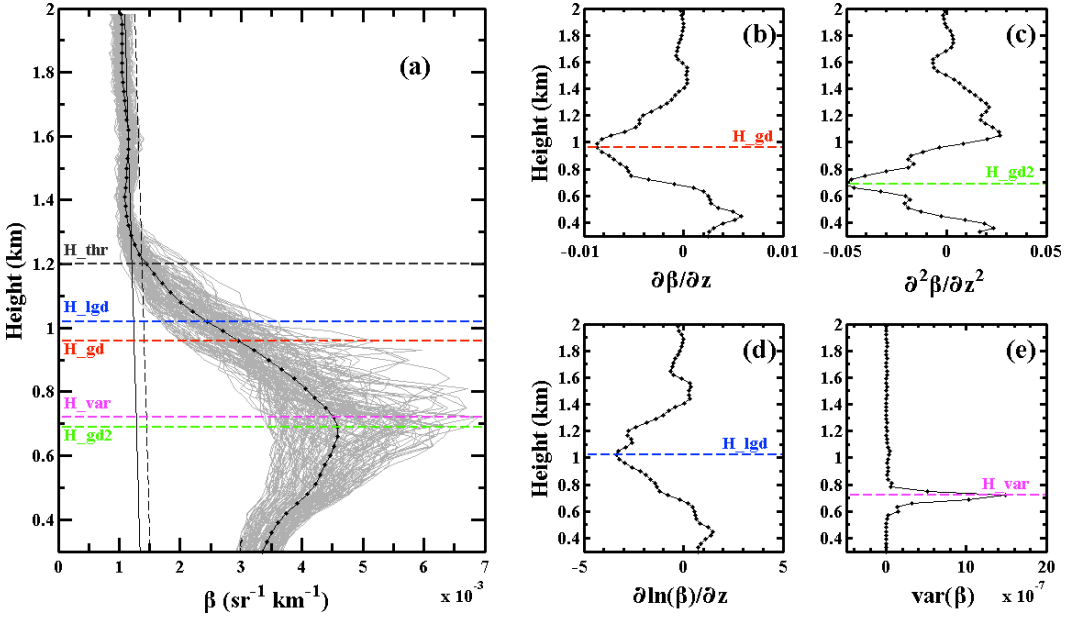

Fig. 1. Comparison of BLH determinations from lidar measurements with five different methods. β denotes the lidar backscatter intensity (sr^{-1} km^{-1}). **(a)** Comparing of BLH derived from different methods. The gray lines are the measured 30 s-averaged β within 1-h centered at 16:30 UTC 24 June 2007 at the SGP site. The black dotted line is the averaged β of all gray lines. H_thr denotes the BLH derived by the threshold method; H_gd denotes the BLH derived by the gradient or derivation method **(b)**; H_gd2 denotes the BLH derived by the second derivation method **(c)**; H_lgd denotes the BLH derived by the log-gradient method **(d)**; H_var denotes the BLH derived by the variance (var) method **(e)** using the data showed as the gray lines in **(a)**.

AMTD
6, 8311–8338, 2013

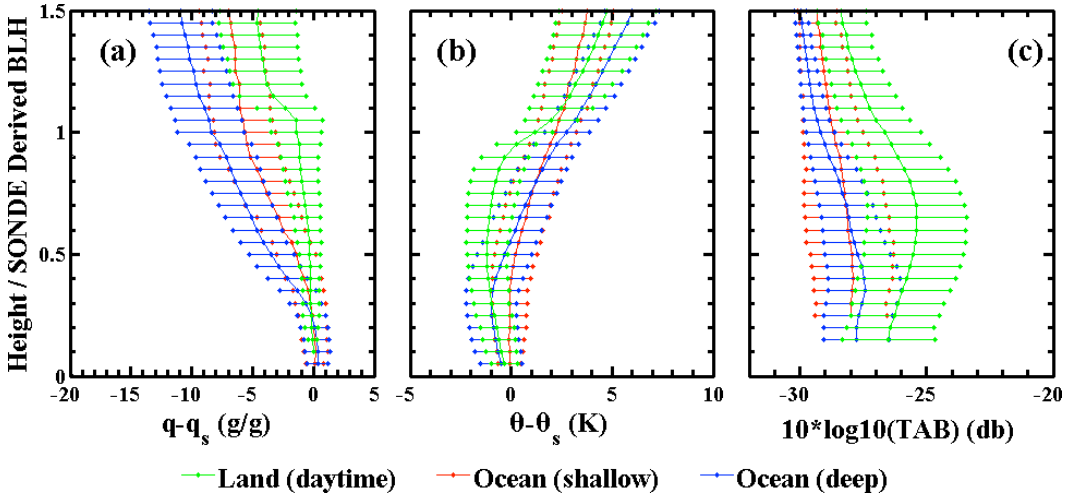

Fig. 2. Comparison of ABL structure in terms of mixing ratio **(a)**, potential temperature **(b)** and TAB **(c)** for over ocean (TWP C2 site, top panel) and land (SGP C1 site, bottom panel). The green and blue line denotes the cases with SONDE-derived BLH between 1.5 and 2 km for land and ocean (deep cases) respectively. The red line denotes the cases with SONDE-derived BLH between 0.8 and 1.2 km for ocean (shallow cases).

AMTD
6, 8311–8338, 2013

Lidar-based remote sensing of atmospheric boundary layer

T. Luo et al.

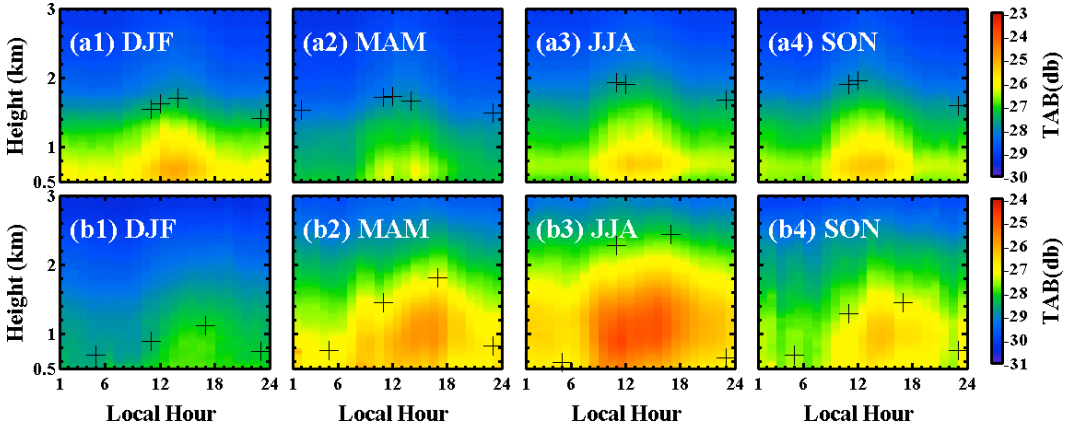

Fig. 3. Diurnal cycle of boundary layer aerosol structure over ocean (TWP C2 site, 2007–2008, top panels) and land (SGP C1 site, 2007–2009, bottom panels). The black dot in each figure represents the BLH derived from SONDE with the *RI* number method.

AMTD
6, 8311–8338, 2013

Lidar-based remote sensing of atmospheric boundary layer

T. Luo et al.

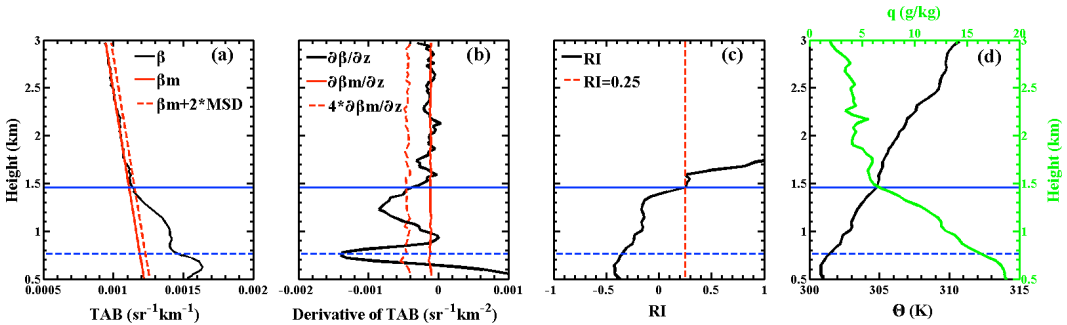

Fig. 4. Illustrations of MPL BLH and MLH identification methods for oceanic measurements: **(a)** TAB; **(b)** TAB gradient; **(c)** *RI*; **(d)** potential temperature and mixing ratio. The blue solid line in each figure denotes the Sonde derived BLH, and the blue dashed line denotes MPL derived MLH.

AMTD
6, 8311–8338, 2013

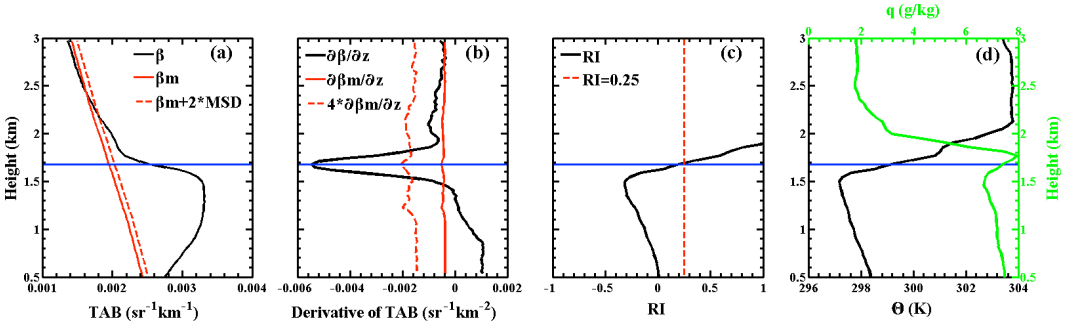

Fig. 5. Illustrations of MPL BLH identification methods for measurements over land during daytime: **(a)** TAB; **(b)** TAB gradient; **(c)** *RI*; **(d)** potential temperature and mixing ratio. The blue line in each figure denotes the Sonde derived BLH.

AMTD
6, 8311–8338, 2013

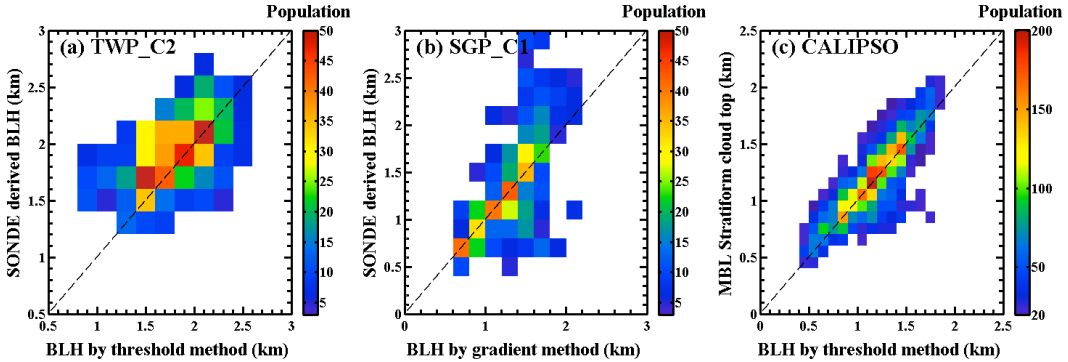

Fig. 6. Comparison of BLHs between SONDE derived and MPL derived **(a)** with the threshold method at TWP_C2 site and **(b)** with the gradient method at the SGP_C1 site; Comparison between marine BLH derived with the threshold method and marine boundary layer stratiform cloud top from CALIPSO measurements **(c)**.

AMTD
6, 8311–8338, 2013

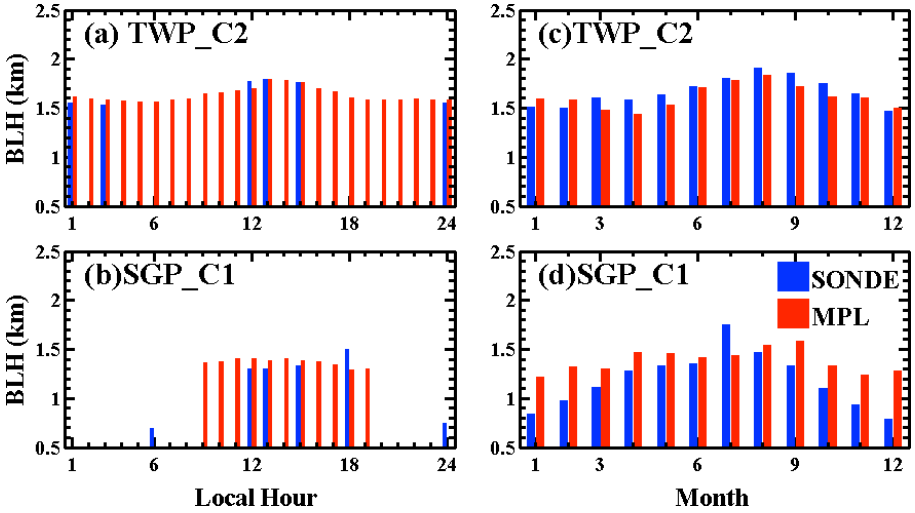

Fig. 7. Diurnal cycles of BLH over ocean **(a)** and land **(b)**; and annual cycles of BLH over ocean **(c)** and land **(d)**.

AMTD
6, 8311–8338, 2013

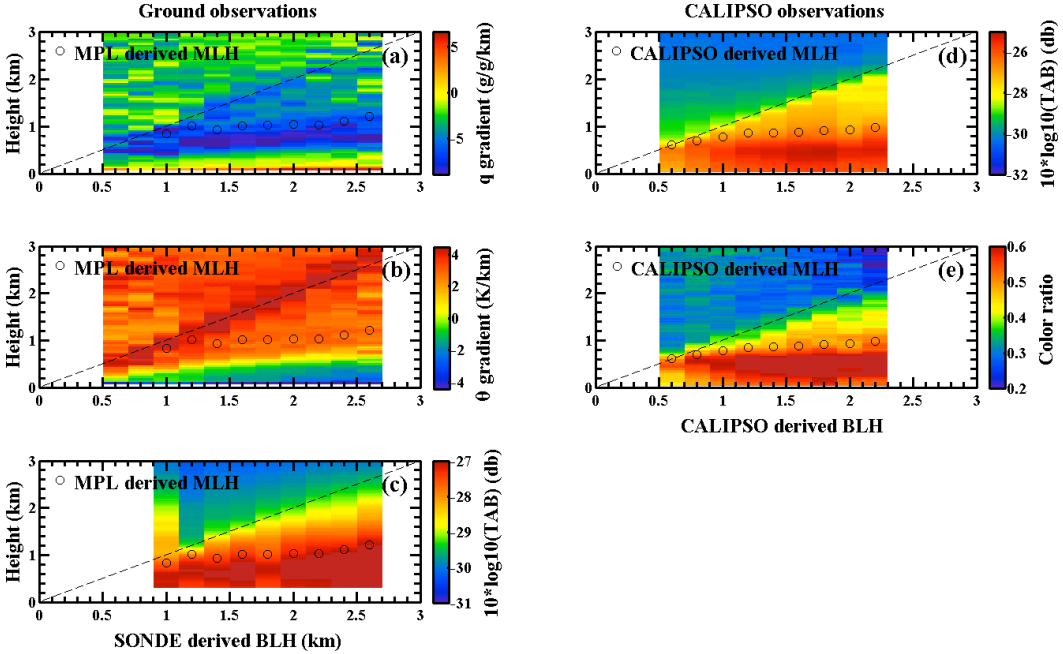

Fig. 8. Left panels: ground based observations at TWP_C2 cite of marine boundary layer decoupled structure in terms of mixing ratio **(a)**, potential temperature **(b)** and TAB **(c)**. Right panels: the same but for satellite based observations near TWP_C2 cite in terms of TAB **(d)** and Color ratio (1024 nm/532 nm) **(e)**.

AMTD
6, 8311–8338, 2013

Lidar-based remote sensing of atmospheric boundary layer

T. Luo et al.